EPJ AP

Applied Physics

EPJ.org

your physics journal

Eur. Phys. J. Appl. Phys. (2016) 74: 30402 DOI: 10.1051/epjap/2016150508

Iron nanoparticles embedded in carbon films: structural and optical properties

Fatemeh Mashayekhi, Azizollah Shafiekhani, and Seyed Ali Sebt

edp sciences

The title “The European Physical Journal” is a joint property of EDP Sciences, Società Italiana di Fisica (SIF) and Springer

Eur. Phys. J. Appl. Phys. (2016) 74: 30402
DOI: 10.1051/epjap/2016150508

THE EUROPEAN PHYSICAL JOURNAL APPLIED PHYSICS

Regular Article

Iron nanoparticles embedded in carbon films: structural and optical properties

Fatemeh Mashayekhi[1,a], Azizollah Shafiekhani[2,3], and Seyed Ali Sebt[1]

[1] Department of Physics, Science and Research Branch, Islamic Azad University, P.O. Box 14665-678, Tehran, Iran
[2] Department of Physics, Alzahra University, Tehran, 1993893973, Iran
[3] School of Physics, Institute for Research in Fundamental Sciences (IPM), P.O. Box: 19395-5531, Tehran, Iran

Received: 10 October 2015 / Received in final form: 11 February 2016 / Accepted: 17 May 2016
Published online: 24 June 2016 –

Abstract. In the present work amorphous hydrogenated carbon films with sputtered iron nanoparticles (Fe NPs @ a-C:H) were deposited by co-deposition of RF-sputtering and RF-plasma enhanced chemical vapor deposition methods using acetylene gas and iron target on quartz and silicon substrates. Samples were prepared in different initial pressures and during constant deposition time. The crystalline structure of Fe NPs @ a-C:H was studied using X-ray diffraction and selected area electron diffraction patterns. The X-ray photoelectron spectroscopy analysis presents that increasing the initial pressure decreases the atomic ratio of Fe/C and the sp^3-hybridized carbon content in prepared samples. The transmission electron microscope image shows the encapsulated Fe NPs in carbon films. The optical properties and localized surface plasmon resonance (LSPR) of samples were studied using UV-visible spectrophotometry, which is shown that increasing of Fe content decreases the intensity of LSPR peak and increases the optical band gap.

1 Introduction

The thin films' science and technology made fundamental progress for understanding the deposition process, microstructure and properties at the nano scale [1–4].

Over the last decades, physical and chemical techniques have been developed for preparation of metal nanoparticles such as, radio-frequency sputtering (RF-sputtering), radio-frequency plasma-enhanced chemical vapor deposition (RF-PECVD), pulsed laser deposition, hydrothermal reduction. All of these methods allow control on the chemical composition and introduction of the lowest possible concentrations of finely dispersed dopants [5,6].

Amorphous hydrogenated carbon (a-C:H) films contain sp^2 and sp^3 C-C bonds and they are well known for interesting properties. They have a width band gap, but it could be engineered by adding metal nanoparticles (Me @ a-C:H) which has attracted a lot of attention in the last two decades. This Me @ a-C:H, on one side has some of the a-C:H properties and on the other side, modifies the a-C:H electrical and magnetic properties. Furthermore, existence of metal into carbon matrix could decrease the strain and also improve the adhesion of a-C:H film on substrates [7–13]. It has also been found that C-C bonds in films altered according to the type of metal. For example Co [11], Ni [6,12] and Cu [13] in a-C:H increase sp^2-C bonds, while Fe increases the sp^3-C bonds and thus increases diamond property of a-C:H films [8,11].

The a-C:H and Me @ a-C:H films have been promising for variety of applications such as automobile industry (gears, valve filters, fuel injector parts, wrist pins and drills) [7,14,15], biomedical industry (orthopedic implants like blood pumps, heart valves and load bearing joints) [16], magnetic storage devices (protection of magnetic hard disks, magnetic recording media and magneto optical recording) [11,17], optical devices (decorative coatings, phase-shift masks and electroluminescence, antireflective coatings for IR windows and solar photovoltaic applications) [8,18,19] and field emission applications (flat panel displays and vacuum microelectronic devices) [11]. Furthermore to date, iron oxide nanoparticles (IONPs) exhibit extensive application in cancer detection and treatment, in the field of oncology. IONPs use as contrast agent for magnetic resonance imaging (MRI) in bioimaging. The cancer cell could be therapeutically heated by activating localized IONPs via an alternating magnetic field. Dong et al. suggested that tumor cell targeting is dominated in vitro by IONPs [20].

Burning up is the main problem of Fe nanoparticles systems when they are put into contact with air due to the strong and fast reactivity of Fe. To avoid such

[a] e-mail: mashayekhi.fatemeh@yahoo.com

a situation, encapsulating Fe-NPs stabilizes the formation of them. Consequently, the NPs present core-shell morphology [8,21].

In this paper, we report a spontaneous process of RF-sputtering and RF-PECVD of Fe NPs @ a-C:H films. The main features of this method like non-wet chemical and room temperature deposition are prior requirements for many applications. Acetylene as carbon source has dual reactive and bombarding gas role in deposition process. The deposition process was studied in the physical sputtering region of iron by variation of gas initial pressure.

2 Experimental details

Fe NPs @ a-C:H thin films were prepared using co-deposition of RF-PECVD systems with 13.56 MHz power supply. The reaction chamber has two electrodes, the smaller one with 5.0 cm in diameter is iron target with 99% purity and the substrate holder is located at larger one with 13.0 cm in diameter. The substrate electrode is grounded by the body of the stainless steel chamber and distance between two electrodes was kept fixed at 5.5 cm. the deposition was carried out on quartz and silicon substrates at room temperature. The basic pressure was about 2.00 ± 0.001 Pa and afterwards the pressure was increased to different initial pressures by acetylene gas flow for deposition while RF power and deposition time were kept fixed at 240 ± 0.1 W and 60 ± 0.1 min, respectively. Figure 1 shows the schematic of experimental set up and details of prepared samples are given in Table 1.

The structural characterization of prepared Fe NPs @ a-C:H thin films with different iron contents was done using X-ray diffraction (XRD) and transmission electron microscope (TEM) analysis. The XRD pattern of samples were recorded by a X-ray diffractometer using Cu-kα radiation in the wavelength of $\lambda = 1.54$ Å. The Philips CM30 microscope was used to obtain TEM image and selected area electron diffraction (SAED) pattern. To study the chemical bond structures the X-ray photo electron spectroscopy (XPS) data of the films were obtained by using Gammadata-scienta ESCA 200 hemispherical analyzer equipped with an Al Kα (1486.6 eV) X-ray source. In the case of optical properties investigation StellarNet EPP-2000 UV-visible spectrometer was applied. On the other hand, the refractive index of films was measured by spectroscopic ellipsometry SE 800.

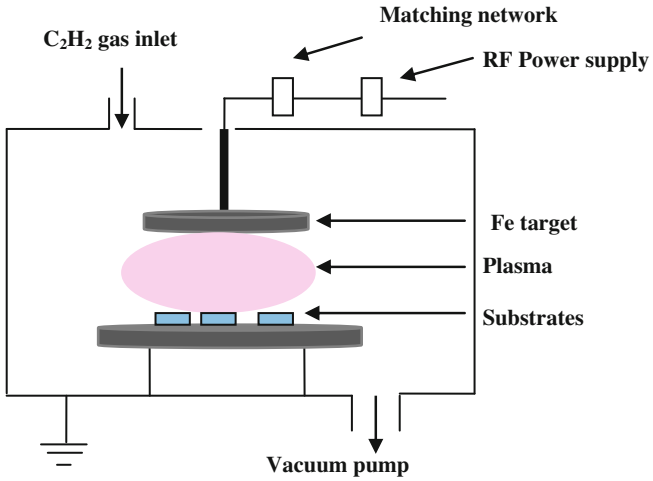

Fig. 1. The scheme of experimental set up and deposition environment with unequal electrodes.

Table 1. Synthesis details of prepared samples.

Sputtering parameters			
Sample	Initial pressure (±0.001 Pa)	Power (±0.1 W)	Time (±0.1 min)
1	2.50	240	60
2	3.00	240	60
3	3.35	240	60
4	3.50	240	60

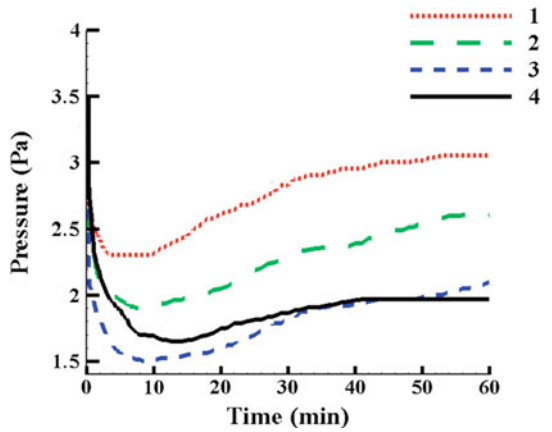

Fig. 2. Monitored pressure as a function of deposition time for samples 1, 2, 3 and 4.

3 Results and discussions

In the case of studying the deposition process, the changes of pressure were recorded in constant power regime during 60 min of each deposition process. Figure 2 shows the time deposition versus the initial pressure.

It is observed that at the beginning of the process (the first 10 min), the pressure strongly decreases to reach a critical pressure between 1.40 and 2.30 Pa, which is related to the high deposition rate of carbon. Then the chamber pressure increases slowly and sputtering of Fe begins, the slow increasing can be due to the simultaneous deposition of hydrocarbon film and Fe NPs.

As it was explained in experimental section, plasma is produced between the electrodes by the RF power. A sheath with an excess of ions is created next to the electrodes due to the higher mobility of electrons rather than ions in the plasma [22]. The sheaths behave like diodes; so the electrodes find dc self-bias voltages. The voltages

ratio is inverse function of the electrode areas as follow:

$$\frac{V_1}{V_2} = \left(\frac{A_2}{A_1}\right)^q, \quad (1)$$

where V_1 and V_2 are voltages of sheath for grounded and powered electrodes and A_1 and A_2 are their areas, respectively. Different values have been reported for q such as $q = 2$ in a capacitive divider state and according to electrodes inverse capacitance [22], $q = 4$ by assumption the collisionless Child-Langmuir law for the sheath dynamic [23,24] and $q = 2.5$, where the sheath dynamics do follow the collisional Child-Langmuir law [24].

In this report a collisional Child-Langmuir law is considered which is much closer to the experimental results ($q = 2.5$). The ratio of the voltage of larger to smaller electrode was calculated 0.008 in our system, with electrodes' diameter of $D_1 = 5$ cm and $D_2 = 13$ cm. Therefore the sheath voltage of powered electrode is almost the same as bias voltage ($V_{\text{bias}} = -(V_1 - V_2)$).

The powered electrode becomes negative with respect to the grounded electrode [22]. Therefore, the positive hydrocarbon radicals are accelerated toward iron target due to its negative sheath potential. On the other hand, the bias voltage for plasma will change with RF power (W) and pressure (P) according to the below equation [22]:

$$V_{\text{bias}} = k\frac{W}{\sqrt{P}}. \quad (2)$$

Which in, k is about 4 as constant coefficient. Based on the above equation, the V_{bias} increase in constant power regime (W).

In order to characterize the structure of synthesized samples, according to the typical XRD pattern given in Figure 3, crystallized α-Fe and Fe oxides (Fe_2O_3 and Fe_3O_4) are formed.

Three peaks at 44°, 65° and 82° are respectively assigned to (1 1 0), (2 0 0) and (2 1 1) indices of α-Fe [8]. The average size of Fe NPs calculated from Scherrer formula is 27 ± 1 nm. With respect to these data, we could say that the surface NPs have core-shell structure. Surface Fe NPs as core surrounded by shell of iron oxides which is embedded in a-C:H.

Typical TEM image of Fe NPs encapsulated in a-C:H is given in Figure 4a. The Fe NPs in the spherical shape are well dispersed in amorphous carbon. The main distribution of particle sizes is about 25 nm which is close to the size founded from Scherrer formula and shown in Figure 4b. The diffraction rings of the SAED pattern and some discrete spotty pattern is shown in Figure 4c. It can be seen there are four diffraction rings that are corresponded to iron oxide (3 2 1) and α-Fe particles (1 1 0), (2 0 0) and (2 1 1). Also, the SAED shows the weak diffraction rings intensity of iron oxide in compare to Fe NPs.

Figure 5 shows the atomic content of the sample's surface from XPS data. The extrapolated data shows that Fe content decreases from 3.90% to 0.05% with increasing the initial pressure from sample 1 to 4. A similar trend is seen for the oxygen content due to oxidization of Fe NPs. while, the carbon content of the films increases with

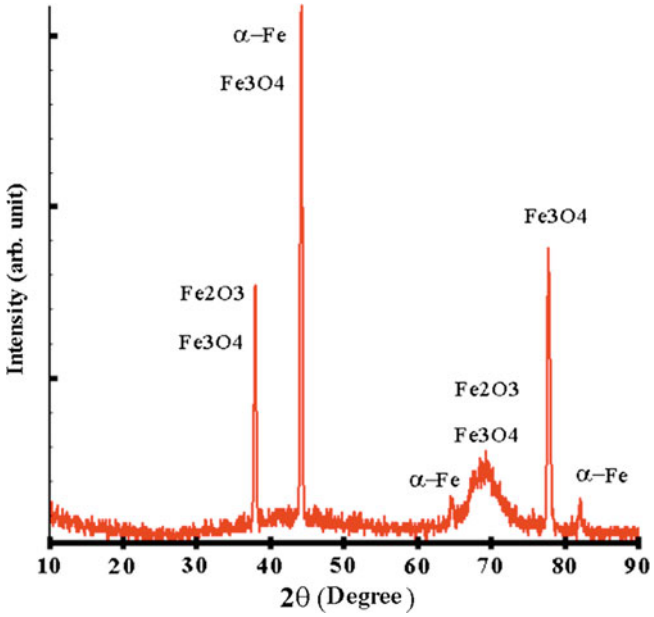

Fig. 3. XRD spectrum of a typical sample shows the crystallized α-Fe and Fe oxides peaks.

increasing initial pressure of samples. These variations are in good agreement with the fact that the rate of deposition is proportional to inverse of the initial pressure according to the equation (3).

Figure 6 shows C 1s peak of XPS spectra for the typical Fe NPs @ a-C:H sample. The main peak at 285 eV with full width at half maximum (FWHM) of about 1.9 eV, is larger than that of diamond (1.45 eV) and graphite (1.35 eV) [25–27]. Therefore, C 1s spectrum is a combination of these two. The broad C 1s peak has been deconvoluted into three peaks which are indicated as peaks A, B and C in Figure 6. These peaks are attributed to the sp^2 and sp^3 bonds of carbon atoms and C-O bond, respectively. The sp^3/sp^2 ratio of the prepared film is calculated by taking into account the area ratio of the sp^3 to sp^2 peaks [25–27]. Table 2 presents the initial pressure, sp^3/sp^2 and Fe/C ratios.

By considering Table 2, we can observe that the sp^3/sp^2 ratio decreases from 1.799 to 0.824 ± 0.0001 and also the Fe/C ratio decreases from 0.061 to 0.007 when the initial pressure increases [8,11]. As the initial pressure is increased, the ionization in the plasma decreases along with the energy of sputtering species ($C_2H_2^+$) [24]. Thus, the sputtering rate of Fe target decreases and more hydrocarbons deposits on the substrate [24,28].

The a-C:H film has intrinsic defects and vacancies due to the synthesis process. Dangling bonds of carbon atoms around the defects and vacancies can provide active sites of Fe atoms direct absorption. On the other hand, environmental oxygens attached to carbon atoms, absorbed Fe atoms due to Fe high oxidation. The Fe atoms also be absorbed indirectly due to the presence of chemical functional groups, such as hydroxyl (–OH) and carboxyl (–COOH) in a-C:H films [29].

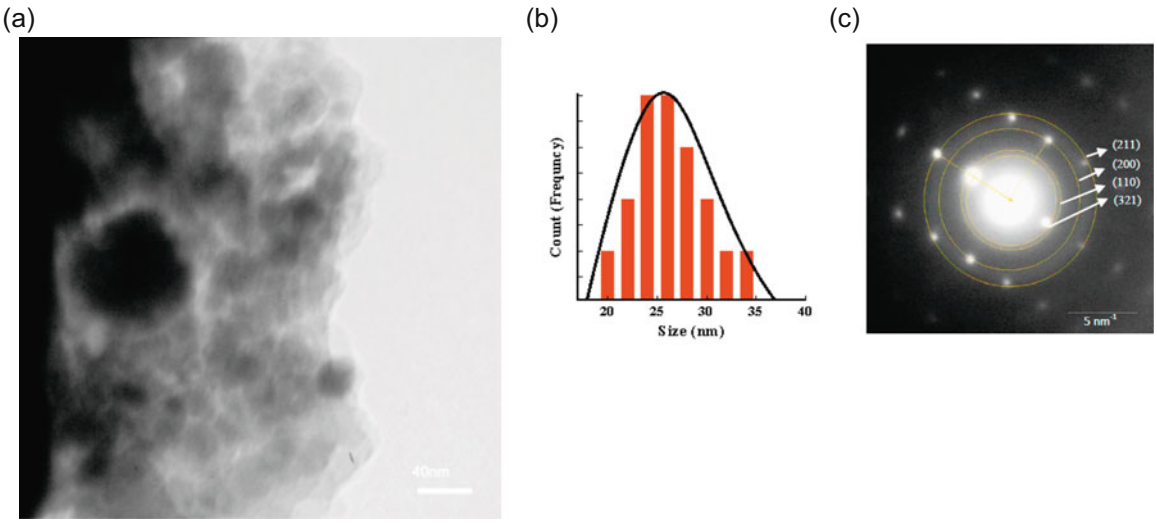

Fig. 4. (a) Typical TEM image shows the Fe NPs in the spherical shape (dark spots) with shell of iron oxides are dispersed in amorphous carbon (gray background), (b) the particle size distribution with average of about 25 nm and (c) electron diffraction pattern of sample shows diffraction rings that are corresponded to α-Fe particles (1 1 0), (2 0 0) and (2 1 1) and iron oxide (3 2 1).

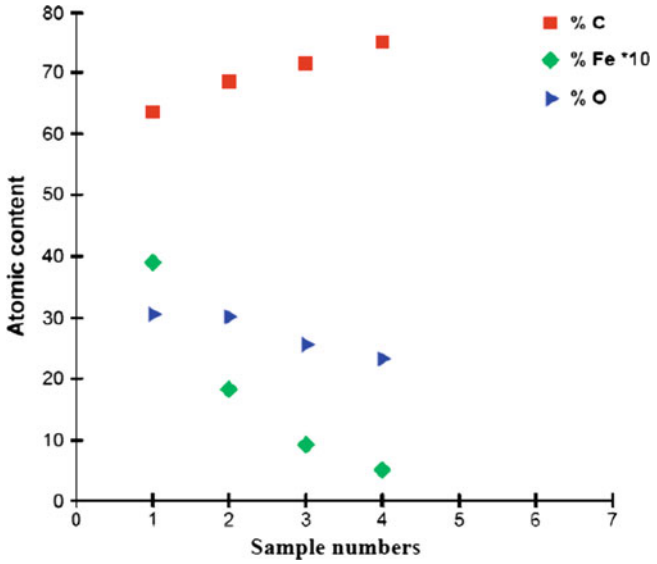

Fig. 5. Iron, carbon and oxygen atomic contents of the as prepared samples collected from XPS data.

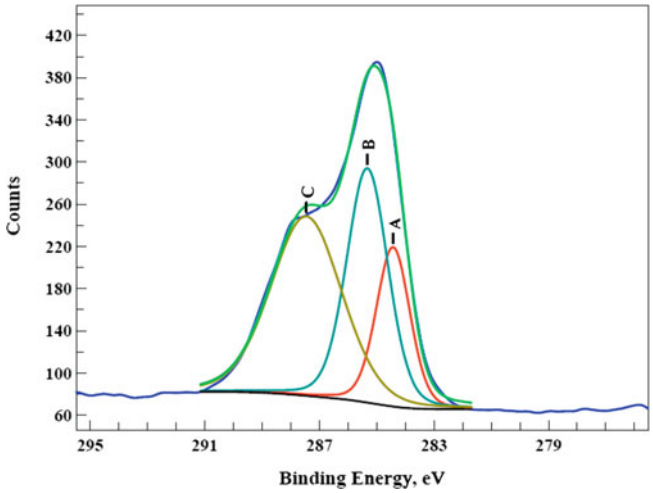

Fig. 6. The typical deconvolution of C 1*s* main peak of sample 1, which shows sp^2 and sp^3 of C-C bonds and C-O bonds as A, B and C peaks respectively.

Table 2. The results of deconvolution of C 1*s* peak as prepared samples.

Sample	Initial pressure (±0.001 Pa)	sp^3/sp^2	Fe/C
1	2.50	1.7990	0.0610
2	3.00	1.3040	0.0170
3	3.35	1.2840	0.0140
4	3.50	0.8240	0.0070

Localized surface plasmon resonance (LSPR) of metal nanoparticles is rapidly developing as non-distinctive technique for the sensing of physical and biological parameters. Most of the applications are based on usage of powder nanoparticles or colloidal. Because of fast oxidation of iron nanoparticle, usually they coated with protective layer. In this circumstance the LSPR of Fe NPs is not easy to detect. The main iron oxides are Fe_2O_3, Fe_3O_4 and FeO which all of them are lossy dielectrics in visible and near infrared. In this sense the real part of these oxides' permittivity is positive and no plasmon can be excited on nanoparticles made of such material [30,31]. The composed nanoparticles on the surface of the synthesized thin film have a core of Fe and shell of iron oxides. So, if somehow the Fe nanoparticle embedded in transparent and protective environment such as a-C:H, the LSPR of Fe NPs could be detected.

The UV-visible absorption spectra of these samples are provided in Figure 7. With respect to above discussion, an absorption peak at 200 nm is due to Fe NPs LSPR [32–34]. The absorption peak in the UV region is principally due to $\pi - \pi^*$ transitions.

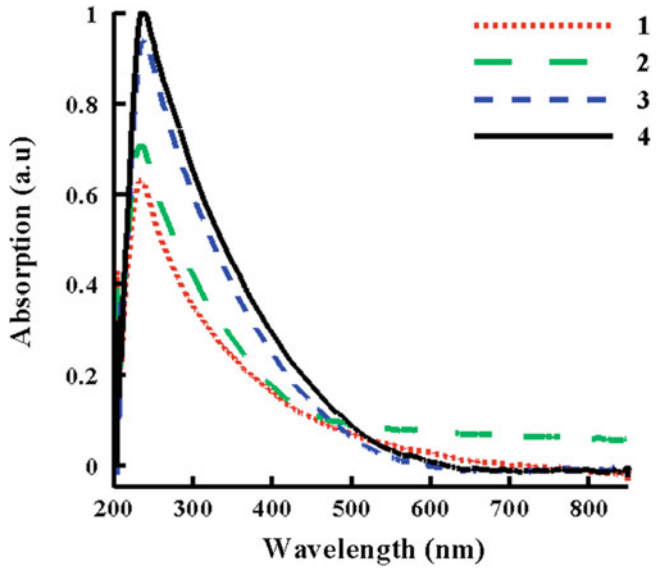

Fig. 7. UV-visible absorption spectra of 1–4 samples, which show the increasing of LSPR intensity as function of initial deposition pressure.

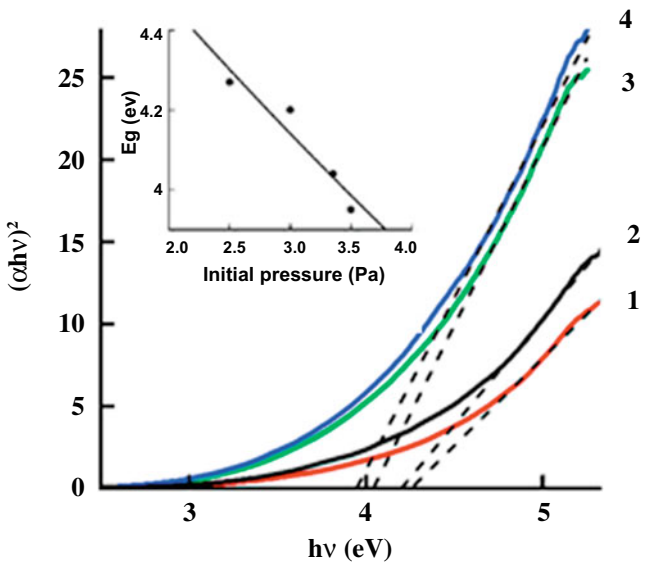

Fig. 8. The optical band gap energies of the synthesized samples with different content of Fe NPs found through Tauc function by extrapolating of tangent line to linear part of spectra, (insert) the band gap of the samples decrease with respect to increase of initial pressure.

It was observed that the intensity of the LSPR peak increased (from 0.63 to 1.00) by increasing the pressure. The LSPR peak intensity increases indicated reduction of the absorption coefficient of samples. It was also realized the absorption coefficient of samples decreased with an increase in the pressure, which has been confirmed by ellipsometric measurements of k (from 0.20 to 0.04). Therefore, the order of LSPR peak intensity represented the order of absorption coefficient of the samples.

The optical band gap energy can be estimated using Tauc equation as follow [35]:

$$\alpha h\nu = \beta(h\nu - E_{\mathrm{g}})^{n}. \tag{3}$$

Where in β is a constant, ν is the transmission frequency, E_{g} is the band gap of the sample and n describes the nature of the band transition. The best fitting with linear part of the spectra was coincided with $n = 1/2$. This indicates a direct allowed transition mechanism [35,36].

Figure 8 shows Tauc plot of as prepared samples, which shows the variation of the optical band gap from 4.27 to 3.95 eV with an increase in the initial pressure from 2.50 to 3.50 ± 0.001 Pa.

In fact, a considerable structural change is induced to leading sp^3 structures in carbon films by increasing iron content. As π states lie closer to Fermi level than σ states, the band gap energy is described transition from filled π states of valence band to empty π states of conduction band. The reduction in the optical band gap energy can be explained by the fact that the fraction of sp^2 bonding will increase and of sp^3 bonding will reduce by a decrease in the Fe content [36], which are in agreement with XPS results. According to Table 2, increasing the initial pressure decreases the amount of Fe and thereby reduces the sp^3/sp^2 ratio. Therefore, the sp^3 content can be arranged according to the band gap of samples. The collected data of initial pressure, LSPR peak intensity, band gap and sp^3/sp^2 ratio have been summarized in Table 3.

Table 3. The LSPR peak intensity, band gap (E_{g}) and C-C sp^3/sp^2 as a function of initial pressure of as prepared samples, which show the consistency of their trends.

		UV-vis		XPS
Sample	Initial pressure (±0.001 Pa)	LSPR peak Intensity (a.u.)	E_{g} (eV)	sp^3/sp^2
1	2.50	0.630	4.270	1.7990
2	3.00	0.720	4.160	1.3040
3	3.35	0.970	4.040	1.2840
4	3.50	1.010	3.950	0.8240

4 Conclusion

Fe NPs @ a-C:H thin films were prepared by co-deposition of RF-sputtering and RF-PECVD methods. Investigation on the deposition and sputtering process shows that the iron content of thin films increases with decreasing the initial pressure of the chamber. The composed NPs have core-shell structure with core of Fe and shell of iron oxides. The XPS characterization indicates that the sp^3–hybridization of Fe NPs @ a-C:H thin films raises by increasing Fe NPs content. The size and concentration of Fe NPs can be tuned by controlling the pressure at constant power and time regimes. TEM image shows encapsulated Fe NPs. UV-visible absorption spectra show that increasing of Fe content decreases the intensity of LSPR peak and increases the band gap of samples. This is consistent with increasing of sp^3 hybridization from XPS study.

References

1. Ş. Ţălu, M. Bramowicz, S. Kulesza, A. Shafiekhani, A. Ghaderi, F. Mashayekhi, S. Solaymani, Ind. Eng. Chem. Res. **54**, 8212 (2015)
2. C. Le Graet, T.R. Charlton, M. McLaren, M. Loving, S.A. Morley, C.J. Kinane, R.M.D. Brydson, L.H. Lewis, S. Langridge, C.H. Marrows, APL Materials **3**, 041802 (2015)
3. D. Babonneau, T. Cabioc'h, M. Denanot, A. Naudon, Appl. Phys. Lett. **74**, 800 (1999)
4. X. Ling, P. Zhang, R. Li, D. Fan, X. Yao, Surf. Interface Anal. **45**, 943 (2012)
5. T. Ghodselahi, M.A. Vesaghi, A. Shafiekhani, Surf. Coat. Technol. **202**, 2731 (2008)
6. A. Usman, M.S. Rafique, M. Khaleeq-ur-Rahman, Mater. Chem. Phys. **126**, 649 (2011)
7. K. Bewilogua, D. Hofmann, Surf. Coat. Technol. **242**, 214 (2014)
8. Sh. Wan, L. Wang, Q. Xue, Electrochem. Commun. **11**, 99 (2009)
9. Ş. Ţălu, S. Stach, T. Ghodselahi, A. Ghaderi, S. Solaymani, J. Phys. Chem. B **119**, 5662 (2015)
10. Ş. Ţălu, S. Stach, S. Solaymani, J. Electroanal. Chem. **749**, 31 (2015)
11. X. Ling, P. Zhang, R. Li, Surf. Interface Anal. **45**, 943 (2013)
12. B. Pandey, D. Das, A.K. Kar, Appl. Surf. Sci. **337**, 195 (2015)
13. N. Dwivedi, S. Kumar, H.K. Malik, J. Phys. Chem. Solids **73**, 308 (2012)
14. Sh. Miyake, T. Saito, Tribol Int. **37**, 751 (2004).
15. T. Liskiewicz, A. Al-Borno, J. Coat. Sci. Tech. **1**, 59 (2014)
16. R.J. Narayan, Diamond Rel. Mater. **14**, 1319 (2005)
17. C. Casiraghia, A.C. Ferrari, J. Robertson, Diamond Rel. Mater. **13**, 1416 (2004)
18. N. Gopinathan, C. Robinson, F. Ryan, Thin Solid Films **355**, 401 (1999)
19. P. Oelhafen, A. Schuler, Sol. Energy **79**, 110 (2005)
20. Ch. NDong, J.A. Tate, W.C. Kett, Plos One **10**, 2 (2015)
21. C.M. Wang, D.R. Baer, J.E. Amonette, Nanotechnology **18**, 255603 (2007)
22. J. Robertson, Mat. Sci. Eng. R **37**, 129 (2002)
23. M. Ohering, *Materials Science of Thin Films Deposition and Structure*, 2nd edn. (Academic Press, San Diego, 2002), p. 215
24. M.A. Lieberman, A.J. Lichteberg, *Principles of Plasma Discharges and Materials Processing*, 2nd edn. (John Wiley & Sons, Inc., Hoboken, New Jersey, 2005), pp. 430–432
25. R. Haerle, E. Riedo, A. Pasquarello, Phys. Rev. B **65**, 045101 (2001)
26. T.Y. Leung, W.F. Man, P.K. Lim, W.C. Chan, J. Non-Cryst. Solids **254**, 156 (1999)
27. X. Yan, T. Xu, G. Chen, S. Yang, Appl. Surf. Sci. **236**, 328 (2004)
28. T. Ghodselahi, M.A. Vesaghi, A. Shafiekhani, A. Baghizadeh, M. Lameii, Appl. Surf. Sci. **255**, 2730 (2008)
29. H.L. Zhuang, G.P. Zheng, A.K. Soh, Comput. Mater. Sci. **43**, 823 (2008)
30. N. Sokolik, O.B. Toon, J. Geophys. Res. **104**, 9423 (1999)
31. A. Schlegel, S.F. Alvarado, P. Wachter, J. Phys. C **12**, 1157 (1979)
32. L. Guo, Q. Huang, X.Y. Li, S. Yang, Phys. Chem. Chem. Phys. **3**, 1661 (2001)
33. A. Bhaumik, S. Samanta, N.K. Mal, Pramana J. Phys. **65**, 855 (2005)
34. S. Basu, D. Chakravorty, J. Non-Cryst. Solids **352**, 380 (2006)
35. R. Kiebach, J.A. Luna-Lopez, O.D. Guilherme, M. Aceves-Mijares, J. Mex. Chem. Soc. **52**, 212 (2008)
36. K. Siraj, M. Khaleeq-ur-Rahman, M.S. Rafique, M.Z. Munawar, Appl. Surf. Sci. **257**, 6445 (2011)